

# Neutrino production from photo-hadronic interactions of the gamma flux from Active Galactic Nuclei with their gas content

J.C. Arteaga-Velázquez

*Instituto de Física y Matemáticas, Universidad Michoacana, Edificio C3, Cd. Universitaria, 58040 Morelia, Michoacan, Mexico*  
 Email: arteaga@ifm.umich.mx

## Abstract

The diffuse neutrino flux from FRI and BL Lac type galaxies generated from interactions of their own  $\gamma$  radiation with the gas and dust at the sources is reported. This  $\nu$ -production channel has not been studied in detail up to now. The calculations are based on individual estimations of the neutrino flux in two nearby AGN's: Centaurus A and M87, assuming the validity of the AGN unification model. The predictions for Centaurus A and M87 involved the parameterization of the measured gamma-ray luminosities and the modeling of the material of the galaxies both based on observations performed by several detectors. No hadronic origin for the TeV photons is assumed. The results show that, although the corresponding  $\nu$  flux ( $E^2\Phi_{\nu+\bar{\nu}} \lesssim 10^{-13} \text{ s}^{-1} \text{ sr}^{-1} \text{ GeV cm}^{-2}$ ) is not competitive at high-energies ( $\epsilon_\nu \gtrsim 1 \text{ TeV}$ ) with that from hadronic models, FRI and BL Lac galaxies with  $\gamma$  emission should be already contributing to the diffuse flux of neutrinos in the universe.

*Keywords:* diffuse neutrino flux, gamma ray emission, photo-hadronic interactions, active galactic nuclei

*This is an author-created, un-copyedited version of an article published in Astroparticle Physics. Astroparticle Physics is not responsible for any errors or omissions in this version of the manuscript or any version derived from it. The definitive published authenticated version is available at doi: 10.1016/j.astropartphys.2012.07.002*

## 1 Introduction

According to particle physics, high-energy neutrino production should be a common phenomenon in several places in the universe. At high-energies an important mechanism of neutrino production is by means of pion photoproduction reactions induced by interactions of cosmic rays with the matter and radiation in the universe, the so called hadronic model. If this picture turns out to be true, a deep connexion among the gamma ray, neutrinos and cosmic rays could be established, which can serve to explore the same object in different

windows and learn about the acceleration mechanism of the most energetic particles in the universe.

By using hadronic interaction models, predictions of high-energy neutrino fluxes for several astrophysical objects can be estimated [1], but they rely on the strong assumption that cosmic rays are accelerated at the sources, which still has to be proven. However, independently of the above scenario and the presence of cosmic rays, there should be secondary mechanisms of neutrino production which may be already at work at astrophysical environments that emit  $\gamma$  radiation. Among such mechanisms are muon pair creation [2] and charged pion production [3] by  $\gamma$ -ray collisions with the ambient radiation, thermal photoproduction of neutrino pairs ( $\gamma e^\pm \rightarrow e^\pm + \nu + \bar{\nu}$ ) [4] and photointeractions of the  $\gamma$ -rays of the source with stellar atmospheres and with the gas and dust surrounding the emission region. Although the associated probabilities for these processes are lower than that for the hadronic channel, these  $\gamma$ -ray mediated collisions should be contributing to the background of high-energy neutrinos in the universe.

In consequence, several astrophysical gamma ray sources should be producing continuously neutrinos through the referred secondary reactions, for example, Active Galactic Nuclei. With the arrival of the *Fermi*-LAT telescope, it has been common to find gamma ray emissions from these kind of sources [5, 6], for example, FRI [7] and BL Lacs [8], which are some special cases of Radio Loud Galaxies [9]. Then it is natural to assume a diffuse flux of high-energy neutrinos in the universe produced by the gamma interactions of these populations of AGN's with their own ambient radiation and material. In this paper, the diffuse  $\nu$  flux from FRI and BL Lac objects produced in  $\gamma P$  interactions of high-energy photons with the gas and dust at source is calculated and compared with some AGN predictions derived from hadronic models of cosmic rays. This channel has not been studied in detail up to now.

Only photo-hadronic interactions will be considered for the present work. The contribution from direct  $\mu$ -pair production with subsequent muon decay will be neglected, since its cross section is small in comparison with that for the hadronic case. In the former,  $\sigma \sim \mu b$  [10] and, in the latter, of the order of  $mb$  [11].

In section 2, the expression for the estimation of the diffuse neutrino flux as a function of the photon luminosity of the sources is presented. Along this paper, it is assumed a standard cosmological scenario with  $h = 0.72$ ,  $\Omega_\Lambda = 0.74$  and  $\Omega_m = 0.26$ . For the calculations, Centaurus A (CenA) and M87 are taken as representative objects. Both AGN's are classified as FRI type galaxies, which in the standard AGN unification scenario [9], correspond to misaligned BL Lac sources. The estimated photon luminosities for a single source are shown in section 3. They are obtained from individual fits to the photon luminosities of Centaurus A and M87 measured with telescopes at Earth and on space.

A relevant quantity for the estimation of the diffuse neutrino flux is the gamma-ray luminosity function (GLF) of the sources. The GLF's for FRI and BL Lac galaxies are presented in section 4. The functions are normalized according to the results of the latest *Fermi*-LAT surveys [5, 12] as it will be described.

The models of matter distribution for FRI and BL Lac galaxies are based on observations of Centaurus A and M87. They are introduced in section 5. In section 6, the neutrino yield for photoproduction reactions is shown. This quantity is calculated using the Monte Carlo program SOPHIA v2.01 [13]. The formula to calculate the total  $\gamma P$  hadronic cross section is also presented in this section. The expression is taken directly from the results of the fits of the COMPETE Collaboration [11, 14].

The estimated diffuse neutrino fluxes are finally shown in section 7. The results are discussed and compared with both limits set by modern neutrino observatories and AGN estimations based on hadronic models. Uncertainties in the flux associated with the observed distribution of photon indexes for BL Lac and FRI type objects will be considered in this part of the paper. Conclusions are presented in section 8.

## 2 The $\gamma$ -ray induced neutrino flux

### 2.1 Production at source

Consider an AGN with a  $\gamma$ -ray emission characterized by a photon spectral luminosity  $L_\gamma(\epsilon_\gamma)$ , where  $\epsilon_\gamma$  is the photon energy, both measured at the source frame. Let's assume, for simplicity, that the position of the gamma-ray source is located at the core of the AGN and that both the gas and dust of the host galaxy are composed of protons, which are at rest. Then, the neutrino spectral luminosity,

$$L_\nu(\epsilon_\nu) = \frac{dN_\nu}{dt d\epsilon_\nu}, \quad (1)$$

produced by the interaction of the gamma-photons with the intergalactic material of the AGN along their path can be estimated as

$$L_\nu(\epsilon_\nu) d\epsilon_\nu = \bar{\Sigma}_H \int_{\epsilon_{\gamma,i}}^{\epsilon_{\gamma,f}} \sigma_{\gamma P}(\epsilon_\gamma) Y^{\gamma P \rightarrow \nu}(\epsilon_\gamma, \epsilon_\nu) L_\gamma(\epsilon_\gamma) d\epsilon_\gamma. \quad (2)$$

Here,  $\bar{\Sigma}_H$  is the angle-averaged column density for target protons (in units of  $\text{cm}^{-2}$ ),  $\sigma_{\gamma P}$  (measured in  $\text{cm}^2$ ) is the  $\gamma P$  cross section at a photon energy  $\epsilon_\gamma$  and  $Y^{\gamma P \rightarrow \nu}(\epsilon_\gamma, \epsilon_\nu)$  is the neutrino yield, which is defined as the number of neutrinos with energy in the region  $d\epsilon_\nu$  around  $\epsilon_\nu$  that a photon with energy in the interval  $[\epsilon_\gamma, \epsilon_\gamma + d\epsilon_\gamma]$  produces after its collision with a proton at rest. In the above expression  $\epsilon_\gamma$  is in TeV, while particle spectral luminosities are in units  $\text{s}^{-1} \cdot \text{TeV}^{-1}$ .

In equation (2), the limits of integration are set in the high-energy regime:  $\epsilon_{\gamma,i} = 10^{-0.8} \text{ GeV}$  and  $\epsilon_{\gamma,f} = 10^6 \text{ GeV}$ , while the neutrino energy covers the interval from  $\epsilon_{\nu,i} = 10^{-5} \text{ GeV}$  to  $\epsilon_{\nu,f} = 10^6 \text{ GeV}$ . Note that, in  $\gamma P$  interactions, the gamma energy threshold for pion photoproduction is  $\epsilon_{\gamma,th} = m_\pi(m_\pi c^2 + 2m_p c^2)/2m_p \approx 10^{-0.8} \text{ GeV}$ , at the laboratory system [15].

Several assumptions have been made to derive equation (2). First, to give a rough estimation of  $L_\nu(\epsilon_\nu)$  at source, the photon spectral luminosity was considered to be isotropic and constant inside the AGN. It was set equal to the measured value at source as derived from Earth observations. In fact, this quantity is associated with the  $\gamma$  photons which escape without interactions from the AGN. In any case, since corrections due to absorption effects should increase the photon spectral luminosity and neutrinos can emerge from regions where photons may not, the quantity evaluated in (2) should be taken as very conservative. For a more realistic estimation, both the position and view-angle dependence of the AGN luminosity should be considered.

In the above equation, the influence of the intergalactic magnetic field, the photon background and the gas at the source on the absorption and energy loss of the parent particles in the  $\nu$ -production chain has been neglected. These phenomena may play an important role close to

the AGN core (see, for example, [16]) reducing the neutrino luminosity. In the worst scenario, the high-energy neutrino production could be suppressed. To estimate in this extreme case the neutrino luminosity, equation (2) will be alternatively evaluated applying a cut around the center of the corresponding gamma-ray source.

The assumption that the target protons are at rest could work for the hot, warm and cold gasses of the interstellar medium (ISM) in the AGN, but not for the gas moving outwards at high relativistic speeds along the jets. For example, the temperature of the gas supply for the central engine of some AGN's has been estimated to be of the order of keV [17, 18, 19], in such a medium, the mean kinetic energy expected for protons is roughly of the same order of magnitude, which results to be small in comparison with the gamma energies considered in this work ( $\epsilon_\gamma > 10^{-0.8}$  GeV). In the case of the jets, material with bulk Lorentz factors  $\Gamma \sim \mathcal{O}(10)$  seems to be present in several AGN's [20, 21], which could imply proton kinetic energies of the order of  $\Gamma m_p c^2 \sim 10$  GeV (if ultra-high-energy acceleration is not considered [22]), that are not negligible in comparison with  $\epsilon_\gamma$ . This situation is important for BL Lac galaxies, where the jets are closely aligned with the line of sight. Here photointeractions with the relativistic gas flowing along the jets are expected to have a major contribution in equation (2).

If both the gamma flux and the relativistic medium are moving outwards, it results in a smaller amount of energy available for neutrino production and, in consequence, in a lower  $\nu$  luminosity than for the situation with stationary gas. The estimation of the neutrino spectral luminosity in this case is carried out by considering the interaction of gamma-photons with a gas characterized by a Lorentz factor  $\Gamma = 10$ , both moving in the same direction. Calculations of the neutrino luminosity are first performed at the rest frame of the gas using formula (2). The result is then Lorentz transformed to the laboratory reference system through the expression

$$L_\nu \left[ \epsilon_\nu = \frac{\epsilon'_\nu}{\Gamma(1-\beta)} \right] = (1-\beta)L'_\nu(\epsilon'_\nu), \quad (3)$$

with  $\beta = \sqrt{1-1/\Gamma^2}$ . The prime stands for quantities measured at the gas rest frame. A similar equation is employed to evaluate the photon spectral luminosity at the reference frame of the jet.

It is clear that more realistic estimations should also include detailed modeling of the photon's and proton's angular distributions of their momenta. But for the purpose of giving a rough estimation of the neutrino flux from AGN's these distributions will be left out of the present calculations.

## 2.2 Diffuse neutrino flux

The extragalactic neutrino background observed at Earth due to FRI objects and BL Lac galaxies was calculated by means of the relation

$$\frac{d\Phi_\nu(\epsilon_\nu^\circ)}{d\Omega^\circ} = \frac{c}{4\pi} \int_0^{z_{max}} dz \frac{1}{H(z)} \int_{\log_{10} \mathcal{L}_\gamma^{min}}^{\log_{10} \mathcal{L}_\gamma^{max}} L_\nu[\mathcal{L}_\gamma, \epsilon_\nu^\circ(1+z)] \cdot \rho_\gamma(\mathcal{L}_\gamma, z) \cdot d(\log_{10} \mathcal{L}_\gamma) \quad (4)$$

where  $L_\nu[\mathcal{L}_\gamma, \epsilon_\nu^\circ(1+z)]$  is the neutrino spectral luminosity of an individual AGN with integrated gamma-ray luminosity

$$\mathcal{L}_\gamma = \mathcal{L}_\gamma(\epsilon_{\gamma_1}, \epsilon_{\gamma_2}) = \int_{\epsilon_{\gamma_1}}^{\epsilon_{\gamma_2}} \epsilon_\gamma \cdot L_\gamma(\epsilon_\gamma) d\epsilon_\gamma, \quad (5)$$

and located at a redshift  $z$ , with  $\epsilon_\nu = \epsilon_\nu^\circ(1+z)$  representing the neutrino energy at source and  $\epsilon_\nu^\circ$  the corresponding particle energy at Earth after adiabatic energy losses due to redshift.  $\rho_\gamma(\mathcal{L}_\gamma, z)$  is the gamma-ray luminosity function (GLF) of the AGN sources per comoving volume  $dV_c$  and interval  $d(\log_{10} \mathcal{L}_\gamma)$ , in units of  $\text{cm}^{-3}$ , while

$$c/H(z) = (c/H_0)[1 - \Omega_m + \Omega_m(1+z)^3]^{-1/2}, \quad (6)$$

where  $H(z)$  is the Hubble parameter at redshift  $z$  and  $c/H_0 = 1.28 \times 10^{28} \text{ cm}$  [11] is the Hubble length. A flat cosmological model dominated by vacuum energy with  $\Omega_\Lambda = 1 - \Omega_m = 0.74$  is assumed. The neutrino background flux is given in units  $\text{s}^{-1} \cdot \text{sr}^{-1} \cdot \text{GeV}^{-1} \cdot \text{cm}^{-2}$ .

### 3 The gamma ray luminosity for a single source

To evaluate  $L_\gamma(\epsilon_\gamma)$  for FRI radio galaxies, the gamma-ray fluxes from Centaurus A and M87 are employed. These sources will be considered as representative ones. Of course, for a more realistic calculation the measured distributions of the spectral indices and integrated luminosities for this kind of sources should be included [23].

Centaurus A and M87 are nearby FRI type objects which have been detected in the MeV-TeV energy regime. The source of the gamma-ray emission has not been identified yet. Astronomical observations indicate that the  $\gamma$  radiation could be produced in the nucleus, the inner jet or radio lobes of the sources [24, 25, 26]. More stringent limits come from combined multi-wavelength observations of M87, which point out that the gamma-ray production site could be located at the nucleus of the AGN [27]. The mechanism behind this emission is also unknown. Both leptonic and hadronic models have been invoked to explain the  $\gamma$ -ray production, however, modern observations are still not able to exclude among the different scenarios (see, for example, [25, 27]).

The closest FRI radio galaxy to the Earth is Centaurus A. It is located at an approximate distance of 3.4 Mpc [28]. Measurements of the  $\gamma$ -ray flux in the interval 0.1 – 1 GeV have been performed with the EGRET detector on board of the Compton Gamma-Ray Observatory [29, 30]. In the 0.1 – 30 GeV energy range, data has been collected with the *Fermi*-LAT instrument [25] and in the very high-energy region ( $\epsilon_\gamma^\circ > 100 \text{ GeV}$ ), with the telescopes of the H.E.S.S. experiment [24]. Centaurus A has an integrated  $\gamma$ -ray flux of  $\Phi_\gamma(\epsilon_\gamma^\circ > 100 \text{ MeV}) = (1.50 \pm 0.45) \times 10^{-7} \text{ ph} \cdot \text{cm}^{-2} \cdot \text{s}^{-1}$  [25].

On the other hand, M87 is found at a distance of 16.7 Mpc from the Earth [27]. Its gamma-ray flux has been measured with the *Fermi*-LAT telescope in the range of 0.2 to 32 GeV and with HEGRA [31], HESS [32] and VERITAS [33] in the energy regime of 0.1 – 30 TeV. Above 100 MeV, the integrated flux of M87 is  $(2.45 \pm 0.63) \times 10^{-8} \text{ ph} \cdot \text{cm}^{-2} \cdot \text{s}^{-1}$ , almost an order of magnitude smaller than that for Centaurus A [26].

Now, let's be  $\Phi_\gamma(\epsilon_\gamma^\circ) = dN_\gamma/dt^\circ d\epsilon_\gamma^\circ dA^\circ$  the differential photon spectrum (in units of  $\text{s}^{-1} \cdot \text{TeV}^{-1} \cdot \text{cm}^{-2}$ ) detected at Earth from Centaurus A or M87. Suppose a steady and isotropic emission, the photon spectral luminosity of the AGN, corrected for redshift energy losses and attenuation due to interactions with the background radiation, is given by

$$L_\gamma(\epsilon_\gamma) = 4\pi D_L^2 \cdot \frac{\Phi_\gamma(\epsilon_\gamma)}{(1+z)^2} \cdot e^{\tau(\epsilon_\gamma, z)}, \quad (7)$$

where  $z$  and  $D_L$  (in cm) are the redshift and luminosity distance to the source, both related

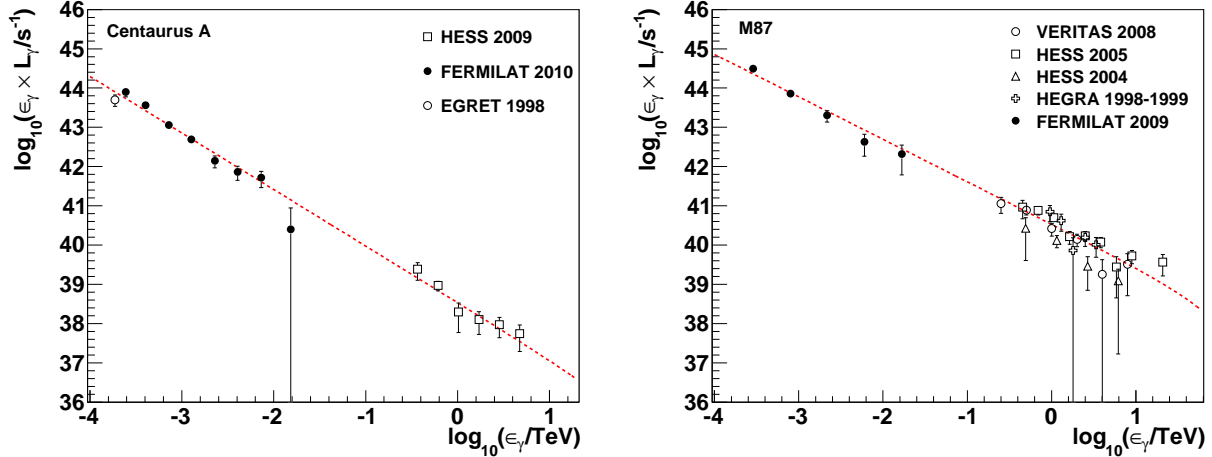


Figure 1: Photon spectral luminosities for Centaurus A (left) and M87 (right) derived from  $\gamma$ -ray measurements performed with different experiments (data points, see text). The results of the fits with formula (9) are shown in each case (segmented lines).

Table 1: Values of the fit parameters  $a$  and  $b$  of formula (9) for Centaurus A and M87.

| AGN         | $\log_{10}[b/s^{-1} \cdot \text{TeV}^{-1}]$ | $a$              |
|-------------|---|------------------|
| Centaurus A | $38.53 \pm 0.09$                            | $-2.44 \pm 0.03$ |
| M87         | $40.53 \pm 0.03$                            | $-2.08 \pm 0.02$ |

through

$$D_L(z) = (1+z) \int_0^z c dz / H(z), \quad (8)$$

and  $\tau(\epsilon_\gamma, z)$  is the  $\gamma\gamma$  optical depth for a photon traveling from the source with initial energy  $\epsilon_\gamma$ . For this work,  $\tau(\epsilon_\gamma, z)$  is extracted from [34].

The photon spectral luminosity for Centaurus A, multiplied by  $\epsilon_\gamma$ , is presented in Fig. 1. It is calculated using  $D_L = 3.4$  Mpc [28] in equation (7) along with the differential photon spectrum as derived from measurements with EGRET [29], HESS [24] and *Fermi*-LAT [25]. In the same figure, the result for M87 is shown. Here  $D_L = 16.7$  Mpc [27] and the data from HEGRA [31], HESS [32], VERITAS [33] and *Fermi*-LAT [26] are taken into account.

To describe the photon spectral luminosities, each graph in Fig. 1 is fitted using a power-law function with a cut-off at high-energies,

$$L_\gamma^{\text{fit}}(\epsilon_\gamma) = b \cdot \left[ \frac{\epsilon_\gamma}{\text{TeV}} \right]^a \cdot e^{-(\epsilon_\gamma/10^2 \text{ TeV})}, \quad (9)$$

where  $a$  and  $b$  stand for the fit parameters. The cut is introduced considering the possibility that the gamma-ray emission could not be of hadronic but leptonic origin (see, for example, [35]). The results of the fit are shown in table 1.

The integrated luminosity above 100 MeV for Centaurus A and M87 is evaluated substituting the values of the fit parameters and formula (9) in equation (5). In the former, it is obtained  $\mathcal{L}_\gamma(\epsilon_\gamma > 100 \text{ MeV}) = 7.2 \times 10^{40} \text{ erg} \cdot \text{s}^{-1}$ , which is more than an order of magnitude lower than in the case of M87 for which  $\mathcal{L}_\gamma(\epsilon_\gamma > 100 \text{ MeV}) = 1.1 \times 10^{42} \text{ erg} \cdot \text{s}^{-1}$ .

Table 2: Values of the parameters of the RLF [36, 37].

| $\log_{10}(\rho_I/\text{cm}^{-3})$ | $\alpha_I$ | $\log_{10}(\mathcal{L}_I/\text{W} \cdot \text{Hz}^{-1} \cdot \text{sr}^{-1})$ | $z_I$ | $k_I$ |
|------------------------------------|------------|---|-------|-------|
| -80.991                            | 0.586      | 26.48   | 0.710 | 3.48  |

Using the photon spectral luminosities of Centaurus A and M87 as a reference, the corresponding luminosity for a single source characterized by an integral luminosity  $\mathcal{L}_\gamma$  can be calculated by means of the formula

$$L_\gamma(\epsilon_\gamma) = L_\gamma^{\text{fit}}(\epsilon_\gamma) \cdot \left[ \frac{\mathcal{L}_\gamma}{\mathcal{L}_\gamma^{\text{fit}}} \right], \quad (10)$$

where  $\mathcal{L}_\gamma^{\text{fit}}$  is evaluated using (9) in equation (5).

The luminosities here derived from Centaurus A and M87 will be also applied for BL Lac galaxies, which is justified by appealing to the AGN unification scheme [9]. In this case, it will be assumed that the gamma ray emission from FRI and BL Lac objects has a common origin and that the respective  $\gamma$ -ray fluxes are isotropic and of equal magnitude.

## 4 The gamma-ray luminosity functions

### 4.1 The GLF for FRI galaxies

The gamma-ray luminosity function (GLF) for FRI radio galaxies used in this work is taken from reference [36]. In that paper, the GLF function is obtained exploiting the correlation between radio and gamma-ray luminosities exhibited by FRI and FRII radio galaxies with  $\gamma$ -ray emission. Once established such a correlation, the radio luminosity function (RLF) determined in [37] for radio loud galaxies is converted to the GLF, which is later normalized according to the source count distribution of  $\gamma$ -ray loud radio galaxies measured with *Fermi*-LAT [12].

The GFL is given by the following expression [36]:

$$\rho_\gamma(\mathcal{L}_\gamma, z) = \kappa [d(\log_{10} \mathcal{L}_{151 \text{ MHz}})/d(\log_{10} \mathcal{L}_\gamma)] \rho_r(\mathcal{L}_{151 \text{ MHz}}, z). \quad (11)$$

where  $\kappa = 0.081 \pm 0.011$  is the normalization factor,  $\mathcal{L}_\gamma$  is the integrated  $\gamma$ -ray luminosity in the interval  $10^{-4} - 10^{-2}$  TeV and  $\mathcal{L}_{151 \text{ MHz}}$  is the 151 MHz monochromatic luminosity in units of  $\text{W}/\text{Hz} \cdot \text{sr}$  [37]. On the other hand,  $\rho_r(\mathcal{L}_{151 \text{ MHz}}, z)$  is the 151 MHz RLF for FRI galaxies, measured in  $\text{cm}^{-3}$  per interval of comoving volume and  $\log_{10} \mathcal{L}_{151 \text{ MHz}}$ . This quantity is determined in reference [37] and it is shown below:

$$\rho_r(\mathcal{L}_{151 \text{ MHz}}, z) = \begin{cases} \eta(z) \rho_I \left( \frac{\mathcal{L}_{151 \text{ MHz}}}{\mathcal{L}_I} \right)^{-\alpha_I} \exp(\mathcal{L}_{151 \text{ MHz}}/\mathcal{L}_I) (1+z)^{k_I} & z \leq z_I, \\ \eta(z) \rho_I \left( \frac{\mathcal{L}_{151 \text{ MHz}}}{\mathcal{L}_I} \right)^{-\alpha_I} \exp(\mathcal{L}_{151 \text{ MHz}}/\mathcal{L}_I) (1+z_I)^{k_I} & z > z_I. \end{cases} \quad (12)$$

The parameters of the RLF are presented in table 2. In the above equation [36]

$$\eta(z) = \frac{d^2 V_w / d\Omega dz}{d^2 V_c / d\Omega dz} \quad (13)$$

is a cosmological conversion factor to compensate for the fact that in [37] a flat universe with  $\Omega_m = 1$  and  $\Omega_\Lambda = 0$  is employed. In formula (13)

$$\frac{d^2V_W}{d\Omega dz} = \frac{c^3 z^2 (2+z)^2}{4H_{0,W}^3 (1+z)^3}, \quad (14)$$

with  $c/H_{0,W} = 1.85 \times 10^{28}$  cm and

$$\frac{d^2V_c}{d\Omega dz} = \frac{c[D_L(z)]^2}{H(z)(1+z)^2}. \quad (15)$$

The relation between  $\mathcal{L}_{151\text{ MHz}}$  and  $\mathcal{L}_\gamma$  is established in [36] through their correlation with the 5 GHz radio luminosity,  $\mathcal{L}_{5\text{ GHz}}$ , where  $\mathcal{L}_f = f \cdot \epsilon_f dN/dtdf$ . Here,  $f$  is the frequency of the radiation and  $\epsilon_f$ , the energy of the associated photon. First, the 151 MHz monochromatic luminosity is transformed to  $\mathcal{L}_{5\text{ GHz}}$  assuming a spectral index  $\alpha_r = 0.8$  for all radio galaxies [37], i.e.  $S_r(f) \propto f^{-\alpha_r}$ , where  $S_r$  is the radio flux density at frequency  $f$ , and then the radio luminosity at 5 GHz is converted to the integrated gamma-ray luminosity using the expression [36]

$$\log_{10}(\mathcal{L}_\gamma/\text{erg} \cdot \text{s}^{-1}) = (-3.90 \pm 0.61) + (1.16 \pm 0.02) \log_{10}(\mathcal{L}_{5\text{ GHz}}/\text{erg} \cdot \text{s}^{-1}). \quad (16)$$

With formulas (11) - (16), the GLF can be already calculated. The limits on  $z$  and  $\mathcal{L}_\gamma$  defined for the gamma-ray luminosity function in [36] are summarized in table 3. These values are used to define the integration bounds of expression (4) in the case of FRI galaxies. The limits on  $\epsilon_\gamma$  in  $\mathcal{L}_\gamma$  are also presented in table 3. Accordingly, they were used to evaluate  $\mathcal{L}_\gamma^{\text{fit}}$  in equation (10). For Centaurus A (M87),  $\mathcal{L}_\gamma^{\text{fit}}(\epsilon_{\gamma 1}, \epsilon_{\gamma 2}) = 6.3 \times 10^{40}$  ( $4.4 \times 10^{41}$ )  $\text{erg} \cdot \text{s}^{-1}$ .

## 4.2 The GLF for BL Lac galaxies

For BL Lac galaxies the gamma-ray luminosity function (GLF) is taken from reference [5]. There, the GLF is calculated on the basis of a sample of 42 BL Lac galaxies detected with the *Fermi*-Lat telescope during its first three months of sky-survey at galactic latitudes  $|b| > 10^\circ$ . The GLF derived by the *Fermi*-LAT Collaboration for BL Lac galaxies per interval of comoving volume and  $\log_{10} \mathcal{L}_\gamma$  is presented below:

$$\rho_\gamma(\mathcal{L}_\gamma, z) = \frac{\rho_B}{\log_{10} e} \left( \frac{\mathcal{L}_\gamma}{10^{48} \text{ erg} \cdot \text{s}^{-1}} \right)^{-\zeta+1}. \quad (17)$$

Here,  $\rho_\gamma$  is measured in  $\text{cm}^{-3}$ .  $\mathcal{L}_\gamma$  is the integrated gamma-ray luminosity for  $\epsilon_\gamma > 100$  MeV. The values of the parameters  $\rho_B$  and  $\zeta$  are estimated in [5] for two different bins of redshift:  $z = 0.0 - 0.3$  and  $z > 0.3$ . The respective values are shown in table 4.

The integration limits for equation (4) are summarized in table 3. They are chosen to cover roughly the luminosity and redshift ranges of the BL Lac sample reported in [5].



Table 3: Limits on  $z$  and  $\mathcal{L}_\gamma$  for the gamma-ray luminosity functions of FRI [36] and BL Lac galaxies [5], and definitions of the  $\epsilon_\gamma$  integration bounds for  $\mathcal{L}_\gamma$ .

| Galaxy | $z_{min}$ | $z_{max}$ | $\mathcal{L}_\gamma^{min} [\text{erg} \cdot \text{s}^{-1}]$ | $\mathcal{L}_\gamma^{max} [\text{erg} \cdot \text{s}^{-1}]$ | $\epsilon_{\gamma_1} [\text{TeV}]$ | $\epsilon_{\gamma_2} [\text{TeV}]$ |
|--------|-----------|-----------|---|---|------------------------------------|------------------------------------|
| FRI    | 0.0       | 5.0       | $1 \times 10^{39}$  | $1 \times 10^{48}$  | $10^{-4}$                          | $10^{-2}$                          |
| BL Lac | 0.0       | 0.3       | $2 \times 10^{44}$  | $1 \times 10^{46}$  | $10^{-4}$                          | $10^5$                             |
| BL Lac | 0.3       | 1.2       | $2 \times 10^{46}$  | $4 \times 10^{48}$  | $10^{-4}$                          | $10^5$                             |

## 5 The gas and dust content of individual sources

### 5.1 Centaurus A

#### 5.1.1 Model for FRI galaxies based on CenA

Due to its proximity to Earth, Centaurus A has been well studied in the literature (see for example, the reviews [38, 39]). To calculate the angle-averaged gas column density,  $\bar{\Sigma}_H$ , traversed by the gamma-ray flux at source, a simple model (called **CenA1**) is built based on the observational data. A sketch depicting the main structures of the model is shown in figure 2. The main parameters are presented in table 5.

The most prominent features of Centaurus A are the nuclear region, the circumnuclear disk, the dust lane, the jets and the halo [38, 39]. All of them, but the jet structures, are included in the model. Accordingly, the corresponding  $\bar{\Sigma}_H$  will be used only for FRI radio galaxies, where the jets are not aligned with the line of sight.

In this model of Centaurus A, the VLBI radio core [40] it is assumed to be the source of the  $\gamma$  radiation. This supposition is not yet confirmed, but it is still consistent with observations. Actually, the observed position of the gamma-ray core encompasses the radio core and the inner kpc jets [24, 25]). An upper limit of  $R = 0.01 \text{ pc} = 3.09 \times 10^{16} \text{ cm}$  has been established for the radius of the source from VLBI observations [40]. But according to some models based on observational data [25, 41] the actual size could be smaller, of the order of  $10^{15} \text{ cm}$ . Here, it will be taken  $R_1 = 0.01 \text{ pc}$ , which is measured from the center of the nucleus of the galaxy. For the gas density, the situation is also uncertain. Assuming free-free absorption in the core of Centaurus A and using data from mm and X-ray observations, in [41] a rough estimation of  $n_H \approx 10^6 \text{ cm}^{-3}$  is given, value that will be used for this work.

X-ray observations of the nucleus of Centaurus A reveals the presence of two spectra with different degrees of nuclear absorption [42]. The spectra could be associated either with the emission of a single X-ray source attenuated by different components of a strong absorber [42, 43, 44] or with the combined emission from the accretion disk and the pc-scale VLBI jet

Table 4: Values of the parameters of the GLF function (17) for BL Lac galaxies and two different redshift bins [5].

| Redshift bin    | $\zeta$ | $\rho_B [10^{-85} \text{ cm}^{-3}]$ |
|-----------------|---------|-------------------------------------|
| $z = 0.0 - 0.3$ | 2.08    | 2.61                                |
| $z > 0.3$       | 2.10    | 1.62                                |

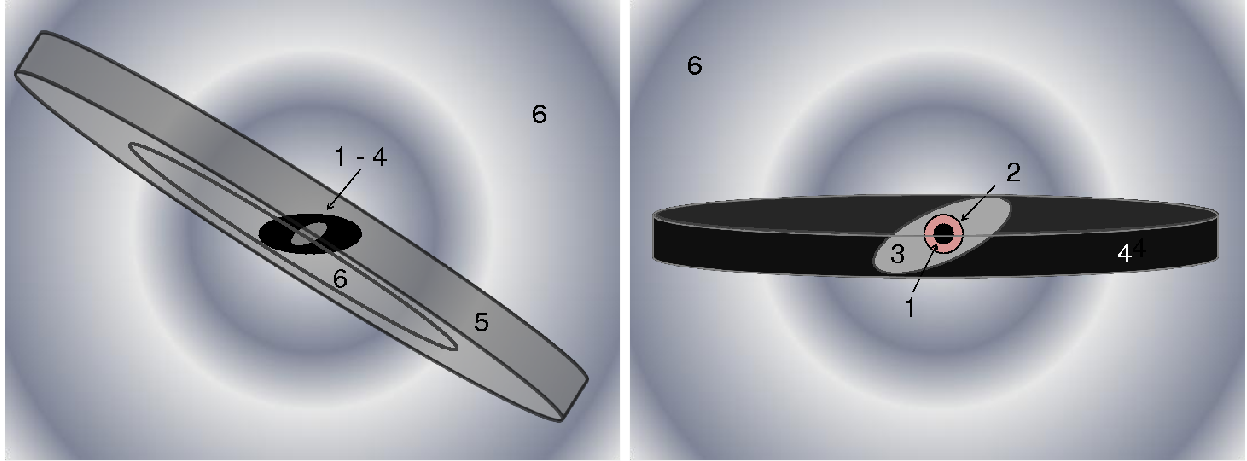


Figure 2: Model **CenA1** for the matter distribution in Centaurus A. In the figures, the following structures are represented: (1) core, (2) X-ray absorber, (3) nuclear disk, (4) circumnuclear disk, (5) dust lane and (6) ISM and halo. On the left, the biggest structures of the galaxy are shown. On the right, a close-up of the inner region of Centaurus A is presented.

[19]. In this paper, the first scenario will be used to get insight into the nuclear environment of Centaurus A. Here, it will be assumed that the absorber is in the form of a cold cloud entirely surrounding the core [45] characterized by a column density with weighted-mean of  $2.4 \times 10^{23} \text{ cm}^{-2}$  (best-fit model from [42]). The cloud is supposed to have a uniform density ( $n_H \approx 8.64 \times 10^5 \text{ cm}^{-3}$ ) and a spherical geometry with radius  $R_2 = 0.1 \text{ pc}$ , which is taken from the estimated emission radius of the Fe  $K\alpha$  lines observed in the X-ray spectra, presumably belonging to the absorber [19]. Although, such a cloud may not be representative of the environments of the AGN (see, for example, discussions in [19, 42, 44]), it is a simple model to deal with that in some degree reproduces the observed column depths.

SINFONI observations of the central region in Centaurus A reveals that the corresponding gas morphology is consistent with a warped-disk structure formed by several inclined rings [46]. Accordingly, the region between  $R_2 = 0.1 \text{ pc}$  and  $R_3 = 40 \text{ pc}$  will be described using the warped-disk model [28, 47]. The position ( $PA$ ) and inclination ( $i$ ) angles<sup>1</sup> for the tilted rings of the model are taken from [46] and are presented in table 6. Since data is reported only between  $0.824 - 31.3 \text{ pc}$  [46], the values of the disk parameters outside this range, but inside  $R = 0.1$  and  $40 \text{ pc}$ , will be kept constant. For simplicity, a disk aspect ratio  $k(R) = h(R)/R = 0.5$  is assumed, where  $h(R)$  is the thickness as a function of the cylindrical radius,  $R$ .

The next important structure of Centaurus A is the circumnuclear disk [38, 39]. Through independent  $CO(1-0)$  absorption measurements against the nucleus [49] and detection of  $CO(2-1)$  emission lines [50], it was found that the gas distribution agrees with a disk-like feature with  $PA = 155^\circ$  and  $i = 70^\circ$ , external radius  $R_4 = 200 \text{ pc}$ , thickness of  $80 \text{ pc}$  and gas mass of  $\sim 10^7 M_\odot$ . The disk has an inner cavity of radius  $R = 40 \text{ pc}$  as suggested by  $H_2$  emission studies towards the core of the galaxy [49]. Following reference [49], a  $n_H \sim r^{-2}$

<sup>1</sup>Here, following reference [48], the  $PA$  is just the angular orientation in the sky of the major axis of the galaxy and it is measured counter clockwise from north to the blue shifted side of the aforementioned axis. On the other hand,  $i$  is the angle of inclination of the galaxy to the line of sight. For an edge-on galaxy,  $i$  is equal to  $90^\circ$ . Meanwhile, for a galaxy with its northern (southern) side closer to the observer, the value of  $i$  lies above (below)  $90^\circ$ .

Table 5: Extension and density distributions of the main gas structures in the model **CenA1**. Here,  $R$  represents the cylindrical radius and  $r$ , the spherical one.

| Structure          | $R$ [pc]                | $n_H$ [cm $^{-3}$ ]                                 |
|--------------------|-------------------------|---|
| Core               | 0.01                    | $10^6$  |
| X-ray absorber     | 0.01 – 0.1              | $8.6 \times 10^5$                                   |
| Nuclear disk       | 0.1 – 40                | $3.4 \times 10^2$                                   |
| Circumnuclear disk | 40 – 200                | $(5.5 \times 10^5)/r^2$                             |
| Dust lane          | $(0.8 - 7) \times 10^3$ | $(3.6 \times 10^{13})/r^4$                          |
| ISM and halo       | $35 \times 10^3$        | $4 \times 10^{-2}[1 + (r/500 \text{ pc})^2]^{-0.6}$ |

density distribution will be assigned to the circumnuclear disk, where  $r$  is the spherical radius. To estimate the density inside the nuclear disk, the above density function is evaluated using  $R = 40$  pc.

A gap in the gas distribution is present between  $R = 200 - 800$  pc as suggested by several studies [28, 50, 51]. Beyond this region, the dust lane is found [38, 39]. A warped-disk model with inclined tilted-rings [52, 53] seems to describe the optical,  $H\alpha$ ,  $CO$  and infrared observations of the dusty disk (see [38] and references therein). The radius of the dust lane is about  $R_5 = 7$  kpc and its mass is of the order of  $1.3 \times 10^9 M_\odot$  [39]. To describe the disk aspect ratio, the model of reference [28] is adopted:  $k(R) = h(R)/R = 0.1(R/824 \text{ pc})^{0.9}$ . The values for the position and inclination angles of the tilted-rings in the dust lane are presented in table 6. They are taken from references [28, 50, 48]. A simple  $r^{-4}$  power-law dependence will be assumed for the density distribution of the dusty disk [28, 53].

Finally, XMM-Newton observations of the hot ISM of Centaurus A in X-rays have revealed the presence of a large-scale gas halo extending at least up to  $R_6 = 35$  kpc [54]. An average gas density was determined in [55] from fits to Chandra and XMM-Newton observations, where it was shown that for  $r \lesssim 10$  kpc, it is well described by a beta model  $n_H = n_0[1 + (r/r_0)^{-1.5\xi}]$  with  $n_0 = 4 \times 10^{-2} \text{ cm}^{-3}$ ,  $r_0 = 500$  pc and  $\xi = 0.40 \pm 0.04$ . This profile will be extrapolated up to  $r = 35$  kpc [54]. Additionally, it will be used to fill out the gaps among the internal structures.

Besides the above model, a second one, named **CenA2**, will be also used, in which the nuclear region is left out. The aim is to include the extreme case in which the parent particles (lepton or hadrons) involved in the  $\nu$ -production chain are completely absorbed in the nuclear zone. For this model, the estimation of the column depth is performed by integrating the proton density for the ISM and Halo inside the interval  $r = 40 - 35 \times 10^3$  pc. The corresponding value will be considered as a lower value for  $\bar{\Sigma}_H$ .

### 5.1.2 Model for BL Lac galaxies based on CenA

Since for this type of galaxies the jet lies along the line of sight of the observer, interactions of the gamma-rays with the matter of the jet should be considered. For this calculation, the target of the  $\gamma$  radiation will be a homogeneous and spherical distribution of relativistic gas flowing outwards (with  $\Gamma = 10$ ) and composed of protons (model **JetCenA**). The radius and density of the gas cloud are set equal to the extension and average hydrogen density of the jet of Centaurus A, respectively. For the former,  $r \sim 4$  kpc [56] and for the latter,

Table 6: Position and inclination angles for the nuclear, circumnuclear and dusty disks. Data are taken from the compilation shown in [48]. The original references are also shown. Extrapolations from the measured data have been applied for the intervals  $r = 0.10 - 0.82$ ,  $31.3 - 40$  pc and  $r = 5.69 - 7$  kpc.

| Nuclear disk [46]                  |                  |                   |           |                  |                   |           |                  |                   |
|------------------------------------|------------------|-------------------|-----------|------------------|-------------------|-----------|------------------|-------------------|
| $R$ (pc)                           | $i$ ( $^\circ$ ) | $PA$ ( $^\circ$ ) | $R$ (pc)  | $i$ ( $^\circ$ ) | $PA$ ( $^\circ$ ) | $R$ (pc)  | $i$ ( $^\circ$ ) | $PA$ ( $^\circ$ ) |
| 0.10 – 0.82                        | 45.0             | 144.0             | 8.41      | 44.0             | 168.9             | 19.5      | 39.7             | 149.3             |
| 0.82                               | 45.0             | 144.0             | 9.40      | 39.5             | 169.0             | 20.8      | 42.5             | 147.8             |
| 1.65                               | 37.6             | 148.5             | 10.4      | 36.1             | 167.2             | 22.1      | 46.7             | 146.8             |
| 2.64                               | 38.8             | 152.1             | 11.4      | 35.1             | 165.2             | 23.4      | 48.9             | 145.1             |
| 3.63                               | 42.2             | 154.8             | 12.5      | 34.2             | 163.5             | 24.9      | 51.6             | 144.0             |
| 4.45                               | 44.5             | 160.5             | 13.5      | 35.2             | 161.7             | 26.4      | 53.6             | 142.8             |
| 5.44                               | 42.3             | 165.4             | 14.7      | 36.9             | 159.8             | 27.9      | 55.6             | 141.6             |
| 6.43                               | 44.1             | 167.8             | 15.8      | 36.8             | 157.0             | 29.5      | 54.6             | 137.9             |
| 7.42                               | 45.7             | 168.5             | 17.0      | 36.2             | 153.8             | 31.3      | 58.9             | 134.9             |
|                                    |                  |                   | 18.1      | 36.8             | 151.1             | 31.3 – 40 | 58.9             | 134.9             |
| Circumnuclear and dusty disks [50] |                  |                   |           |                  |                   |           |                  |                   |
| $R$ (pc)                           | $i$ ( $^\circ$ ) | $PA$ ( $^\circ$ ) | $R$ (kpc) | $i$ ( $^\circ$ ) | $PA$ ( $^\circ$ ) | $R$ (kpc) | $i$ ( $^\circ$ ) | $PA$ ( $^\circ$ ) |
| 40 – 200                           | 70.0             | 155.0             | 0.80      | 85               | 94                | 1.09      | 84               | 118               |
|                                    |                  |                   | 0.84      | 84               | 97                | 1.14      | 85               | 121               |
|                                    |                  |                   | 0.89      | 82               | 102               | 1.19      | 88               | 124               |
|                                    |                  |                   | 0.94      | 82               | 107               | 1.24      | 90               | 127               |
|                                    |                  |                   | 0.99      | 82               | 111               | 1.29      | 93               | 128               |
|                                    |                  |                   | 1.04      | 83               | 115               | 1.34      | 96               | 130               |
|                                    |                  |                   |           |                  |                   | 1.38      | 100              | 131               |
| Dusty disk [28]                    |                  |                   |           |                  |                   |           |                  |                   |
| $R$ (kpc)                          | $i$ ( $^\circ$ ) | $PA$ ( $^\circ$ ) | $R$ (kpc) | $i$ ( $^\circ$ ) | $PA$ ( $^\circ$ ) | $R$ (kpc) | $i$ ( $^\circ$ ) | $PA$ ( $^\circ$ ) |
| 1.40                               | 104.8            | 132               | 1.81      | 118.5            | 125               | 2.23      | 110.2            | 127               |
| 1.48                               | 110.3            | 131               | 1.90      | 117.9            | 125               | 2.31      | 107.6            | 127               |
| 1.57                               | 114.5            | 129               | 1.98      | 116.7            | 125               | 2.39      | 105              | 127               |
| 1.65                               | 117.1            | 127               | 2.06      | 114.9            | 126               | 2.47      | 102.6            | 126               |
| 1.73                               | 118.3            | 126               | 2.14      | 112.7            | 127               |           |                  |                   |
| Dusty disk [48]                    |                  |                   |           |                  |                   |           |                  |                   |
| $R$ (kpc)                          | $i$ ( $^\circ$ ) | $PA$ ( $^\circ$ ) | $R$ (kpc) | $i$ ( $^\circ$ ) | $PA$ ( $^\circ$ ) | $R$ (kpc) | $i$ ( $^\circ$ ) | $PA$ ( $^\circ$ ) |
| 2.72                               | 105.5            | 126.9             | 3.21      | 94.2             | 117.4             | 4.86      | 90               | 105               |
| 2.97                               | 99.6             | 125               | 4.04      | 90               | 110.3             | 5.69      | 90               | 102               |
|                                    |                  |                   |           |                  |                   | 5.69 – 7  | 90               | 102               |

$n_H = 1.7 \text{ cm}^{-3}$  [57], both values were derived from X-ray observations performed with the Chandra telescope.

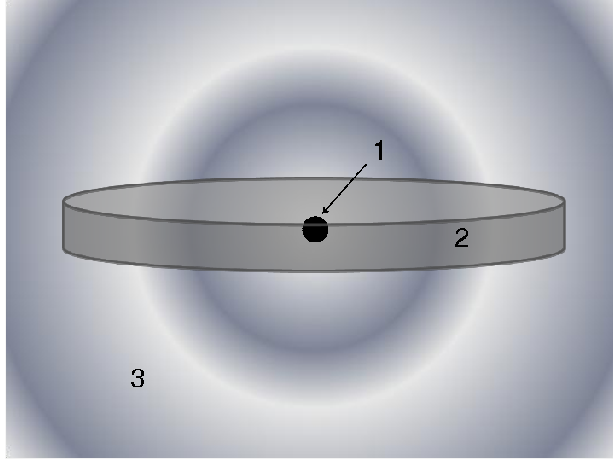


Figure 3: Model **M87a** for the matter distribution of the radio galaxy M87. In the figure, the following structures are represented schematically: (1) core, (2) nuclear disk, and (3) ISM and halo.

## 5.2 M87

### 5.2.1 Model for FRI galaxies based on M87

M87 is one of the closest radio galaxies to Earth, therefore it has become the target of several astronomical observations dedicated to get a deeper understanding of the astrophysics and structure of this type of galaxies. Observations of M87 reveal the presence of a core [58], a nuclear disk [59], a kpc jet [60, 61] and a halo [62, 63, 64]. To build the model for M87, as it was the case for Centaurus A, the contribution of the jet will be neglected.

The source of gamma rays in this model (**M87a**), will be located at the core of the radio galaxy in accordance with the results of the 2008 multi-wavelength on M87 [27]. The results show evidence in favor of a correlation between the radio core and the TeV emissions. Assuming that the first source is located in the central region of the galaxy, it is concluded that the gamma radiation should be produced in the immediate vicinity of the black hole [27]. Following the model proposed in [26] to explain the *Fermi*-LAT MeV/GeV observations on the basis of synchrotron self-Compton emissions from electrons at the core, a gamma source with a radius of  $r_1 = 1.4 \times 10^{16} \text{ cm} = 4.5 \times 10^{-3} \text{ pc}$  is assumed. This value is consistent with both the limits derived from VLBA observations at 43 GHz [65, 66] and the constraints obtained with HESS [67], MAGIC [68] and VERITAS [69] from the observed variability (of the order of a few days) of the TeV radiation. The density of the source is uncertain. Here, the value  $n_H = 10^6 \text{ cm}^{-3}$  will be used, which is in agreement with the limits presented in [70] for the plasma density at the nucleus of M87 and with estimations derived in [71] from the nuclear emission lines measured with the instruments on board of the Hubble Space Telescope (*HST*) in the optical and UV regions, when data is interpreted within the framework of photoionization scenarios.

M87 has a nuclear disk of ionized gas and radius  $r \sim 100 \text{ pc}$  rotating around a massive central object as revealed by the *HST* [59, 72]. The disk has a spiral structure, which seems to be connected with large-scale filaments of gas ( $\sim 1 \text{ kpc}$  long) [59, 72]. These warped structures will not be considered in the present work. The major axis position angle and the inclination of the disk are  $PA = 6^\circ$  and  $i = 35^\circ$ , respectively [73]. Regarding the mean surface density of the disk, a rough estimation of  $\Sigma_H = 2.5 \times 10^{19} \text{ cm}^{-2}$  was obtained in [74] within the central

Table 7: Extension and density distributions of the main gas structures in the model **M87a**. Here,  $R$  represents the cylindrical radius and  $r$ , the spherical one.

| Structure    | $R$ [pc]          | $n_H$ [ $\text{cm}^{-3}$ ]                                 |
|--------------|-------------------|--|
| Core         | 0.0045            | $10^6$   |
| Nuclear disk | 100               | 3.24   |
| Halo         | $260 \times 10^3$ | $4.2 \times 10^{-2} [1 + (r/7.87 \text{ kpc})^2]^{-0.654}$ |

70 pc using data from the HST [59]. In reference [71], the total column density of neutral hydrogen in the disk was constrained to the interval  $\Sigma_H = 10^{19} - 10^{20} \text{ cm}^{-2}$  by combining optical, UV, X-ray and HI 21 cm observations of the nucleus of M87. The presence of cold molecular gas ( $H_2$ ) could largely increase the column density of gas. From observations of the nucleus of M87 with the Submillimeter Array an upper limit  $\Sigma_{H_2} \leq 4.5 \times 10^{22} \text{ cm}^{-2}$  was found in [75] within  $\sim 100$  pc. For the present work, a mean column density of  $\Sigma_H = 10^{20} \text{ cm}^{-2}$  in a plane perpendicular to the disk will be assumed. The nuclear disk will be modeled using a thin disk with radius  $r = 100$  pc and thickness of 10 pc as in reference [75].

The mass and matter distribution of the hot gas in the halo of M87 has been well studied in the literature in the X-ray window with several space observatories, for example, Einstein (see [64] and references therein), ROSAT [76] and XMM-Newton [77]. In reference [78], using X-ray measurements obtained with the Einstein observatory, the density profile of the ISM in the halo of M87 was derived up to a distance of 392 kpc from the nucleus. The distribution was estimated assuming a gas in hydrostatic equilibrium with a spherical distribution described by a beta model  $n_H = n_0 [1 + (r/r_0)^{-1.5\xi}]$ . The corresponding analysis gave the following parameter values:  $n_0 = 4.2 \times 10^{-2} \text{ cm}^{-3}$ ,  $r_0 = (7.87 \pm 1.36) \times 10^3$  pc and  $\xi = 0.436 \pm 0.008$ . The above formula will be incorporated to the present model of M87 in order to describe the matter distribution of the halo up to  $r = 260$  kpc, where the measured gas is still associated with M87 [78]. A figure, showing the main components of M87 here discussed, is presented in figure 3. The parameters of the model are shown in Table 7.

Another model, called **M87b**, will be included into the calculations of the neutrino flux, which does not involve the nuclear region. The column depth in this case is calculated solely from the beta model for the ISM and halo density, from  $r = 40$  to 260 kpc. This model is introduced to derive a lower limit on the column density of target protons for an extreme scenario where the parent particles of neutrinos are completely absorbed before decaying in the internal regions of the AGN.

### 5.2.2 Model for BL Lac galaxies based on M87

Proceeding similarly to the case of Centaurus A, a spherical cloud of gas with homogeneous density and composed of protons will be considered (model **JetM87**). The gas is flowing outwards with Lorentz factor  $\Gamma = 10$ . The radius of the cloud will be  $r = 2$  kpc, which is the length of the jet of the giant radio galaxy M87 [61], and the density,  $n_H \approx 1 \text{ cm}^{-3}$ , as in reference [79]. To end this section the angle-averaged column densities of protons estimated for the models already presented are summarized in table 8.

Table 8: Column depths calculated for Centaurus A and M87 using different models (see text). **JetCenA** and **JetM87** will be employed for the description BL Lac galaxies, while the rest of the models, for FRI objects.

|   | CenA1              | CenA2 | JetCenA | M87a  | M87b | JetM87 |
|---|--------------------|-------|---------|-------|------|--------|
| $\bar{\Sigma}_H(10^{21} \text{ cm}^{-2})$ | $4.58 \times 10^2$ | 0.21  | 20.98   | 16.93 | 2.79 | 6.17   |

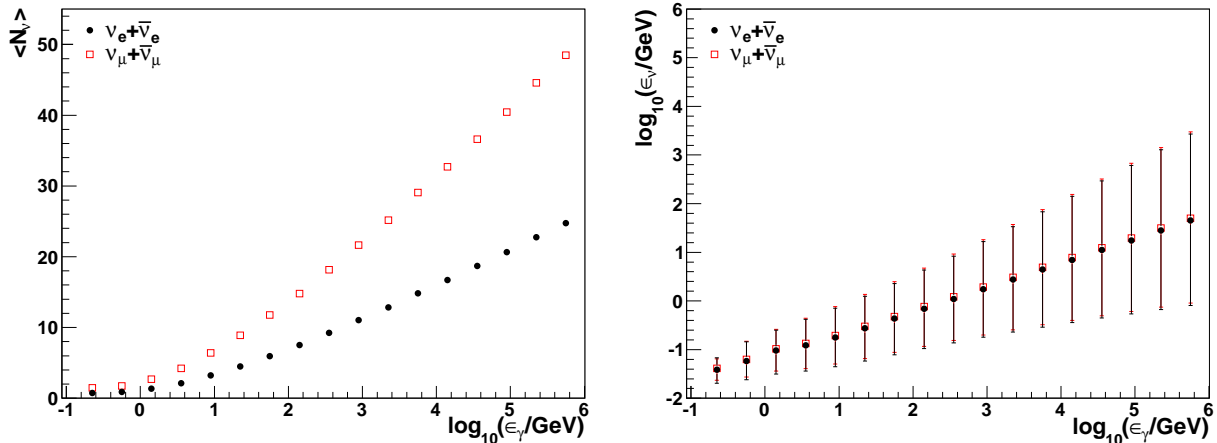


Figure 4: Left: Average electron (muon) neutrino and antineutrino multiplicities for  $\gamma P$  collisions. Right: Median of the neutrino and antineutrino energy distributions for  $\gamma P$  reactions. Error bars represent the 84% and 16% quantiles.  $\epsilon_\gamma$  is the energy of the incident photon.

## 6 The $\gamma P$ hadronic cross section and the neutrino yields

For the calculation of the total  $\gamma P$  hadronic cross section above  $\sqrt{s} = 5 \text{ GeV}$  the following expression is employed [11, 14]:

$$\sigma_{\gamma P} = \delta \cdot Z + \delta \cdot B \log^2(s/s_0) + Y(s_1/s)^{\eta_1}. \quad (18)$$

where  $\sqrt{s}$  is defined as the center-of-mass energy and  $\sqrt{s_1}$  is fixed at 1 GeV. On the other hand,  $\delta = 0.00308$ ,  $Z = 35.45 \text{ mb}$ ,  $B = 0.308 \text{ mb}$ ,  $Y = 0.0320 \text{ mb}$  and  $\eta_1 = 0.458$ , while  $\sqrt{s_0} = 5.38 \text{ GeV}$  [11]. These parameters were obtained by the COMPETE Collaboration by means of a global fit to current accelerator data with  $\sqrt{s} \geq 5 \text{ GeV}$  [14], where the multi-pion production channel is the dominant one. Since, formula (18) can not be applied below  $\sqrt{s} = 5 \text{ GeV}$ , interpolation techniques will be applied on the total cross section data presented in [11] to get  $\sigma_{\gamma P}$  up to 1 GeV. It is in this low-energy regime, where baryon resonances and direct-pion production processes become also relevant [13, 80].

The neutrino yields are obtained using the Monte Carlo program SOPHIA v2.01 [13]. Estimates are performed only for electron and muon neutrinos, since these neutrino flavors are more copiously produced than tau neutrinos in  $\gamma P$  interactions in the energy regime considered in this work. To obtain the neutrino yield  $Y^{\gamma P \rightarrow \nu_\ell}(\epsilon_\gamma, \epsilon_\nu)$ , a 2D histogram is built. Horizontal and vertical axes correspond to the logarithm of the photon and neutrino energies, respectively. The energy intervals involved are  $\log_{10}(\epsilon_\nu/\text{GeV}) = [-5, 6]$  and  $\log_{10}(\epsilon_\gamma/\text{GeV}) = [-0.8, 6]$ , while the size of the bins is to  $\Delta \log_{10}(\epsilon_\nu/\text{GeV}) = 0.1$ .

The bin  $(i, j)$  is filled with the average number of neutrinos,  $\nu_\ell$ , and antineutrinos,  $\bar{\nu}_\ell$ , with energy in the interval  $\Delta \log_{10}(\epsilon_{\nu,j})$  produced per  $\gamma P$  interaction at photon energies  $\epsilon_{\gamma,i}$  in the

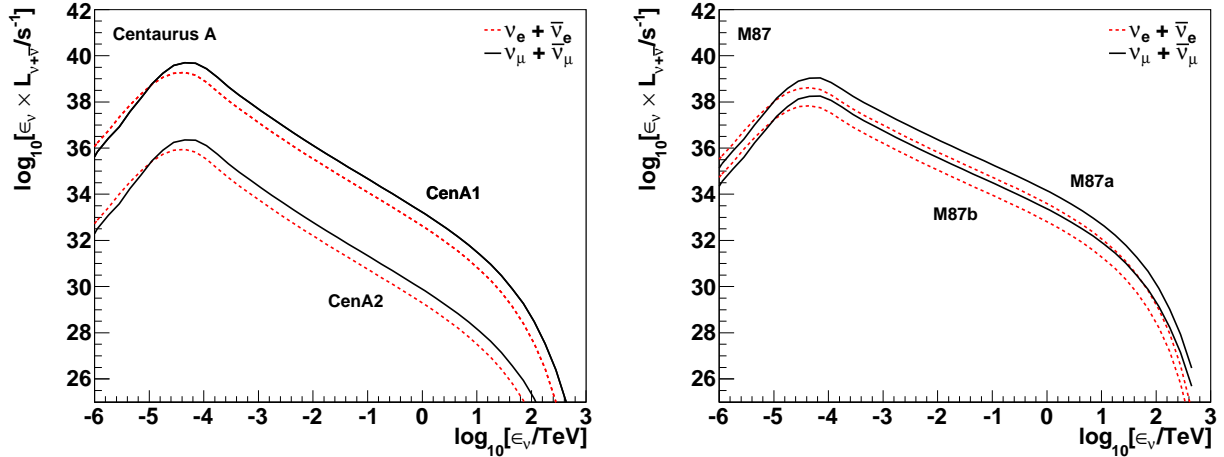


Figure 5: Electron (dotted line) and muon (solid line) neutrino luminosities expected from Centaurus A (left) and M87 (right) at source and produced by interactions of their own  $\gamma$  radiation with the gas and dust in the corresponding galaxies. Different models for the gas and dust content in Centaurus A and M87 are considered (see text and table 8).

laboratory frame. Protons are considered to be at rest in the same reference system. Finally, for each photon energy,  $\epsilon_{\gamma,i}$ , around  $10^5$  events are simulated.

The mean multiplicity and the average energy of neutrinos and antineutrinos in  $\gamma P$  hadronic interactions are presented in fig. 4 versus the photon energy as estimated from the neutrino yields.

## 7 Results

### 7.1 Neutrino flux from CenA and M87

The electron and muon neutrino luminosities at source for Centaurus A and M87, as estimated with formula (2), are presented in Fig. 5. Luminosities are shown for different column depths of target protons: **CenA1**, **CenA1**, **M87a** and **M87b**. It can be seen that neutrino luminosities exhibit a single power law behavior only interrupted at low energies ( $\epsilon_\nu \sim 10^{-4}$  TeV) by a small bump that emerges as a result of the enhancement of the cross section due to the production of hadronic resonances in  $\gamma P$  interactions. At high-energies, at approximately  $\epsilon_\nu = 10$  TeV, the  $L_{\nu+\bar{\nu}}$  functions are limited by an exponential cut, which is generated by the equivalent one for the parent  $\gamma$ -ray luminosities - see equation (9). On the other hand, neutrino luminosities are restricted at low energies by the pion photoproduction energy threshold.

The integrated neutrino luminosities above 100 MeV derived for Centaurus A from fig. 5 are  $\mathcal{L}_{\nu+\bar{\nu}}(\epsilon_\nu > 100 \text{ MeV}) \approx 10^{35} - 10^{32} \text{ erg} \cdot \text{s}^{-1}$ , for electron or muon neutrinos. Meanwhile, regarding the giant elliptical galaxy M87, it is found that  $\mathcal{L}_{\nu+\bar{\nu}}(\epsilon_\nu > 100 \text{ MeV}) \approx 10^{35} - 10^{34} \text{ erg} \cdot \text{s}^{-1}$ . The above integrated luminosities are quite low values.

From the particle luminosities at source, the flux of neutrinos observed at Earth can be



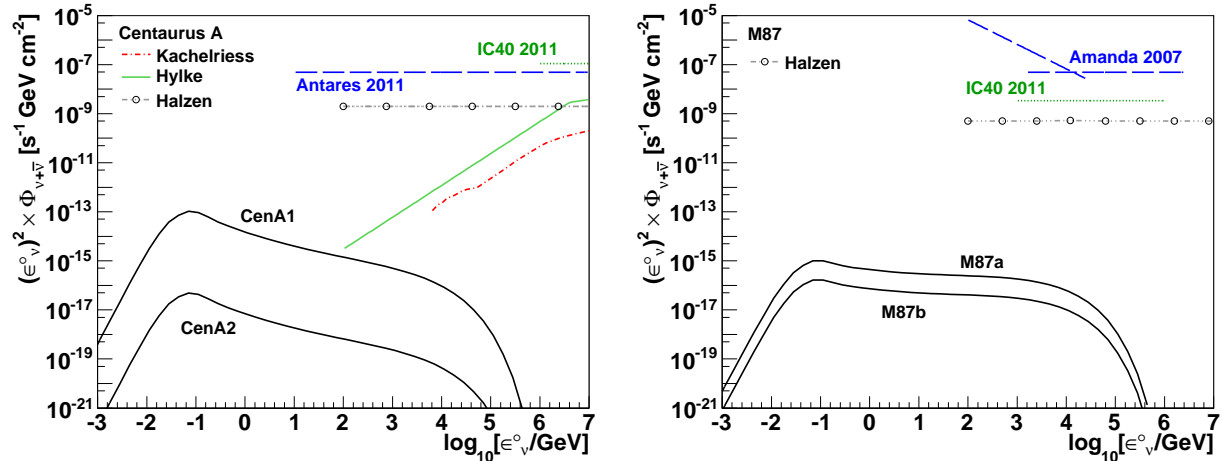


Figure 6: Neutrino and antineutrino fluxes expected from Centaurus A (left) and M87 (right) at Earth for each neutrino type. The flux is produced by interactions of their own  $\gamma$  radiation with the gas and dust at the sources. Different models for the target material in Centaurus A and M87 are considered (see text). Neutrino oscillations are taken into account. Individual 90% C.L upper limits on the neutrino fluxes established with the Amanda [82], ICECUBE [83] and Antares [84] detectors for each galaxy are also shown. For M87, two different  $\nu$  limits from Amanda are shown (segmented lines). They were estimated assuming different spectral indices for the differential  $\nu$  flux:  $\gamma = -2$  and  $-3$  (horizontal and inclined lines, respectively) [82]. Finally, predictions for Centaurus A based on three different hadronic models (Kachelriess [57], Hylke [85] and Halzen [86, 87]) are plotted (left) along with one theoretical estimation for M87 (right, Halzen [86, 87]).

estimated using the formula:

$$\Phi_{\nu+\bar{\nu}}(\epsilon_\nu^\circ) = \frac{(1+z)^2}{4\pi D_L^2} \cdot L_{\nu+\bar{\nu}}(\epsilon_\nu) \quad (19)$$

where  $\epsilon_\nu^\circ = \epsilon_\nu/(1+z)$  is the measured neutrino energy. If neutrino oscillations are taken into account [81], a flux ratio of the form  $(\nu_e + \bar{\nu}_e):(\nu_\mu + \bar{\nu}_\mu):(\nu_\tau + \bar{\nu}_\tau) = 1 : 1 : 1$  should be expected at Earth. Considering this effect upon propagation, the resulting neutrino fluxes, for each flavor, from Centaurus A and M87 are as shown in figure 6. In the same graph, the 90% confidence level upper bounds for neutrino fluxes from Centaurus A and M87 obtained by the Antares[84], Amanda[82] and ICECUBE[83] Collaborations are presented. From figure 6, it is clear that the predicted neutrino fluxes from  $\gamma P$  interactions of high-energy radiation with gas and dust at the sources are too low to be observed, more than six orders of magnitude below the modern experimental limits for the aforementioned AGN's.

In figure 6 (left panel), the expected  $\nu$  fluxes from Centaurus A in the framework of three different hadronic models are also shown for comparison. In all cases, the cosmic ray fluxes (composed by protons) are normalized using the data from the Pierre Auger observatory [88]. One model, due to Hylke et al., assumes that acceleration takes place at the jets [85]. The second model, worked out by Kachelriess et al., invokes cosmic ray acceleration close to the core (with spectral index  $\alpha = 2.7$ ) [57]. The last model, proposed in [86], uses also the  $\gamma$ -ray data from the HESS detector [89] to put an upper limit on the neutrino flux assuming a pionic origin of the TeV radiation. This limit is also applied in [87] to M87 (see right panel of figure 6) by noting that luminosities from Centaurus A and M87 are similar at TeV energies. It is clear from Fig. 6 that at high-energies, relevant for neutrino astronomy

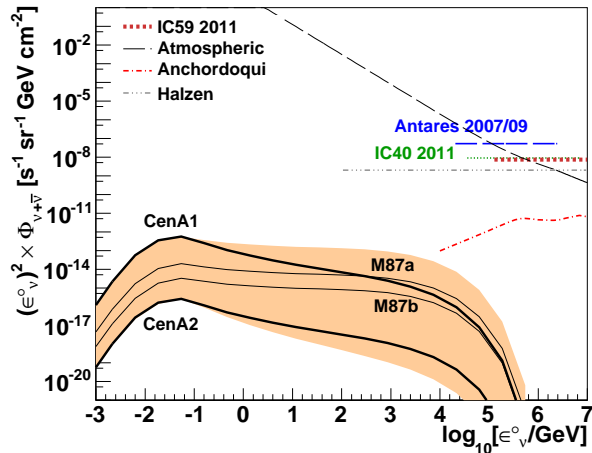


Figure 7: Diffuse flux of neutrinos (for each type) expected from FRI galaxies assuming different  $\nu$  luminosities at the source. Individual luminosities are based on the predicted  $L_{\nu+\bar{\nu}}$  functions of figure 5 for Centaurus A (bold solid lines) and M87 (thin solid lines). Neutrino oscillation is taken into account. The 90% C.L. upper limits on the diffuse neutrino flux derived by the ICECUBE [90, 91] and the Antares [92] collaborations are shown. For comparison, the diffuse flux of atmospheric neutrinos (segmented line)[93], including the prompt component from  $D$ -meson decays [94], is also represented. Two predictions for the diffuse  $\nu$  flux from AGN’s using hadronic models (Anchordoqui [95] and Halzen [86]) are included in the plot. The shadowed band covers the results obtained by varying the photon index (from  $a = -2.08$  to  $-2.67$ ) and the angle-averaged column depths (FRI models of table 8).

( $\epsilon_\nu \gtrsim 1$  TeV), neutrinos from the cosmic ray channel dominate over the modest contribution from  $\gamma P$  interactions studied in this paper.

## 7.2 Diffuse neutrino flux from FRI galaxies

The diffuse flux of neutrinos expected from FRI type galaxies, as derived from equation (4), is shown finally in figure 7. Several curves are obtained, assuming that the individual  $\nu$  luminosities of FRI type galaxies are similar to the ones estimated for Centaurus A or M87 (see figure 5). In this way, the diffuse neutrino fluxes here obtained share the same cuts and spectral shapes exhibited by the individual fluxes considered as reference models. The aforementioned results are compared in figure 7 with the corresponding 90% C.L. limits established with the Antares and ICECUBE neutrino detectors. It is found that the predicted diffuse fluxes are more than seven orders of magnitude lower than the above experimental bounds inside the common energy range. Therefore, the estimated fluxes are outside the reach of the modern neutrino telescopes.

The diffuse flux derived for FRI type radio galaxies is also shown in figure 7 along with two predictions for the background flux of neutrinos from AGN’s based on hadronic models with ultra high-energy protons [86] and iron nuclei [95], respectively. It can be observed that the diffuse  $\nu$  fluxes produced in the framework of hadronic models are dominating the high-energy range over the  $\nu$  flux generated by interactions of the  $\gamma$  radiation with gas and dust at source.

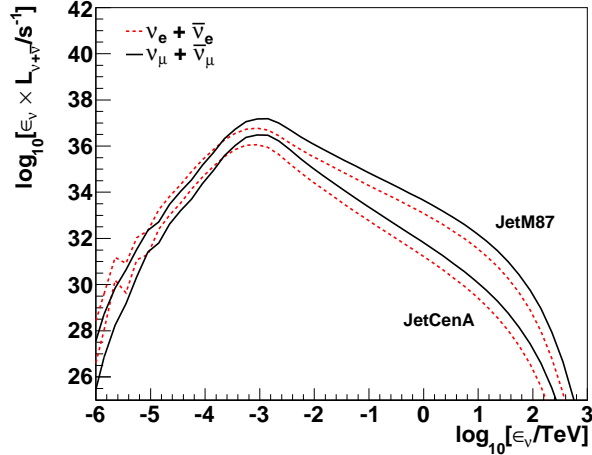


Figure 8: Electron (dotted line) and muon (solid line) neutrino luminosities at source expected from the BL Lac models **JetCenA** and **JetM87**.

### 7.3 Diffuse neutrino flux from BL Lac galaxies

In figure 8, the  $\nu_e$  and  $\nu_\mu$  luminosities at source, calculated with the BL Lac models **JetCenA** and **JetM87**, are shown. They are estimated following relations (2) and (3). As the FRI plots, the above graphs also display a depletion at high-energies (arising from the corresponding cut in the parent  $\gamma$ -ray spectrum), a bump and the effect of the pion photoproduction energy threshold at low energies. However, the last two features are slightly shifted to higher energies, when compared with the FRI luminosities, due to the fact that the target protons are moving outwards the gamma source at relativistic speeds ( $\Gamma = 10$ ). In this regard, the bump is now located at  $\epsilon_\nu \sim 10^{-3}$  TeV. Luminosities are lower in these BL Lac models than for their FRI counterparts. For the models **JetCenA** and **JetM87**, it is obtained that  $\mathcal{L}_{\nu+\bar{\nu}}(\epsilon_\nu > 100 \text{ MeV}) \approx 10^{34} - 10^{33} \text{ erg} \cdot \text{s}^{-1}$  and  $\approx 10^{35} - 10^{34} \text{ erg} \cdot \text{s}^{-1}$ , respectively.

The diffuse neutrino fluxes expected at Earth from BL Lac galaxies are shown in figure 9. Estimations are performed for the models **JetCenA** and **JetM87** and take into account neutrino oscillations. From fig. 9, it can be noticed that the expected fluxes are more than eight orders of magnitude below the present experimental limits at energies above  $3 \times 10$  TeV. That will very likely make these diffuse neutrino fluxes inaccessible for experiments like ICECUBE [90, 91] or the future KM3NET [96].

### 7.4 Uncertainties from the photon index

One can still change the photon index,  $a$ , which appears in formula (9), inside the observable limits and modify the corresponding column depths to obtain error bands for the fluxes from FRI and BL Lac galaxies. For example, for FRI type objects  $a = 2.39 \pm 0.28$  [36]. By varying this parameter inside the allowed interval (including the values reported in table 1) and by changing the magnitudes of the angle-averaged column depth for FRI galaxies (using the models **CenA1**, **CenA2**, **M87a** and **M87b**), then the error band for the corresponding diffuse flux of FRI objects is obtained (see figure 7). In the most optimistic case, the diffuse flux is of the order of  $(\epsilon_\nu^\circ)^2 \Phi_{\nu+\bar{\nu}} \approx 10^{-13} \text{ s}^{-1} \text{ sr}^{-1} \text{ GeV cm}^{-2}$ , however, it is still too low to be detected. For the BL Lac population detected by *Fermi*-LAT,  $a = 1.99 \pm 0.22$  (rm) [5]. By

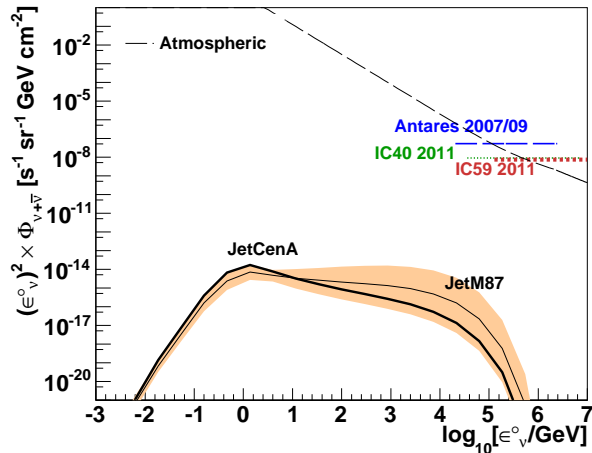


Figure 9: Diffuse neutrino flux for each  $\nu$  species from BL Lac type galaxies (models **JetCenA** and **JetM87**). The 90% C.L. upper limits on the diffuse neutrino flux derived by the ICECUBE [90, 91] and the Antares [92] Collaborations are shown. For comparison, the diffuse flux of atmospheric neutrinos (segmented line)[93], including the prompt component from  $D$ -meson decays [94], is also presented. The shadowed band covers the results obtained by varying the photon index,  $a$ , from  $-1.77$  to  $-2.44$  and the angle-averaged column depths (BL Lac models of table 8).

repeating the above procedure for this kind of AGN's (in the framework of models **JetCenA** and **JetCenA2**), an error band is also obtained for the respective diffuse neutrino flux (see figure 9). Considering this band, it is found that in the most optimistic case the diffuse flux for BL Lacs can reach values of the order of  $(\epsilon_\nu^0)^2 \Phi_{\nu+\bar{\nu}} \approx 10^{-14} \text{ s}^{-1} \text{ sr}^{-1} \text{ GeV cm}^{-2}$ . As before, the situation is neither improved for this type of sources.

Therefore, the conclusion remains the same, the neutrino flux from  $\gamma$ -ray interactions in FRI and BL Lac galaxies is well out of the reach of current and future neutrino telescopes. But even in the case that a large enough detector is ever built with sensitivity to the limits quoted above, it will remain the problem of the atmospheric neutrino background, which is orders of magnitude larger. To see a contribution from both FRI and BL Lac neutrino fluxes against such a background will require a huge amount of neutrino events. The same problem will be faced when looking for an excess of gamma-ray induced neutrinos from the direction of the individual sources Centaurus A and M87. That will require a very large amount of detected events.

## 8 Conclusions

The detection of gamma rays from several FRI and BL Lac galaxies together with the presence of gas and dust at the sources suggest that those objects should emit neutrinos through  $\gamma P$  interactions and contribute to the neutrino background in the universe. However, it was shown that the corresponding diffuse neutrino flux is quite small (in the best case of the order of  $E^2 \Phi_{\nu+\bar{\nu}} \lesssim 10^{-13} \text{ s}^{-1} \text{ sr}^{-1} \text{ GeV cm}^{-2}$ ) and orders of magnitude below the atmospheric neutrino background. Therefore, it will escape observation from modern and future neutrino telescopes. If the observed TeV radiation from FRI and BL Lac sources is of leptonic origin, the diffuse neutrino flux presents a cut around 10 TeV. Additionally, this background is

bounded at low energies by the pion photoproduction energy threshold. Calculations were performed using as references the two nearest FRI galaxies to the Earth: Centaurus A and M87, for the gamma ray spectra and the gas and dust contents of FRI and BL Lac type objects. The validity of the AGN unification scenario was assumed.

Predictions for Centaurus A and M87 were also performed. Despite the proximity of these objects, the present estimations indicate that the neutrino flux produced by the channel here explored will be not observable at observatories like ICECUBE or the KM3Net and in other future experiments. By modifying, in the present calculations, the photon index of the individual sources inside the available experimental ranges, the situation does not improve. In this way, if neutrinos are ever detected from FRI and BL Lac galaxies, the  $\nu$  production by the hadronic model is favoured.

Estimations are still dependent on the real position of the  $\gamma$  ray source at the AGN and on the real shape of the  $\gamma$ -ray spectra in the inner regions of the galaxy. If energy losses of the parent leptonic or hadronic particles in the  $\nu$ -chain are negligible, the biggest contribution results when the source is located close to the massive object that feeds the AGN, hypothesis that at the moment it is not in contradiction with the multi-wavelength observations of the elliptical galaxy M87.

## Acknowledgments

The author thanks R. Engel for his suggestions on the Monte-Carlo programs for photo-hadronic interactions. J.C. Arteaga is also grateful to Claus Grupen and Arnulfo Zepeda for reading the manuscript and the helpful discussions to improve it. The author also thanks the unknown reviewers for many useful suggestions. This work has been partially supported by the Coordinación de la Investigación Científica de la Universidad Michoacana.

## References

- [1] J.K. Becker, Physics Reports 458 (2008) 173-246.
- [2] S. Razzaque et al., Phys. Rev. D 73 (2006) 103005.
- [3] C. D. Dermer and G. Menon, High Energy Radiation from Black Holes: Gamma Rays, Cosmic Rays, and Neutrinos, Princeton University Press, 2009.
- [4] H.Y. Chiu, R.C. Stabler, Phys. Rev. 122 (1961) 1317. V.I. Ritus, JETP 14 (1962) 915. G. Beaudet et al., Phys. Rev. 154 (1966) 1445.
- [5] A.A. Abdo et al., ApJ 700 (2009) 597, arXiv: 0902.1559v1.
- [6] A.A. Abdo et al., ApJ, 707 (2009) 1310, arXiv: 0910.4881v1.
- [7] B.L. Fanaroff and J.M. Riley, MNRAS 167 (1974) 31P.
- [8] P.A. Strittmatter et al., ApJ 175 (1972) L7.
- [9] C.M. Urry and P. Padovani, PASP 107 (1995) 803.

- [10] F. Halzen, K. Hikasa and T. Stanev, Phys. Rev. D34, (1986) 2061.
- [11] K. Nakamura et al. (Particle Data Group), Review of particle physics, J. Phys. G 37 (2010) 075021.
- [12] A.A. Abdo et al., ApJ 720 (2010) 435.
- [13] A. Mücke, R. Engel, J.P. Rachen, R.J. Protheroe, and T. Stanev, Comp. Phys. Commun. 124 (2000) 290, arXiv: 9903478.
- [14] J.R. Crudell et al. (COMPETE Collab.), Phys. Rev. D65 (2002) 074024.
- [15] R.J. Protheroe and P. A. Johnson, Astrop. Phys. 4 (1996) 253, arXiv: 9506119.
- [16] J.P. Rachen and P. Mészáros, Phys. Rev. D58 (1998) 123005, arXiv: 9802280v2.
- [17] S. W. Allen et al., Mon. Not. R. Astron. Soc. 372 (2006) 21.
- [18] D. A. Evans et al., ApJ 642 (2006) 96, arXiv:0512600.
- [19] D. A. Evans et al., ApJ 612 (2004) 786.
- [20] K.I. Kellermann et al., ApJ 609 (2004) 539.
- [21] M.L. Lister, AJ 138 (2009) 1874.
- [22] F.A. Aharonian, MNRAS 332 (2002) 215.
- [23] A.A. Abdo et al., ApJ 707 (2009) 1310.
- [24] F. Aharonian et al., ApJ 695 (2009) L40, arXiv: 0903.1582.
- [25] A. A. Abdo et al., ApJ 719 (2010) 1433, arXiv: 1006.5463.
- [26] A. A. Abdo et al., ApJ 707 (2009) 55, arXiv: 0910.3565.
- [27] The VERITAS Collaboration, the VLBA 43 GHz M87 Monitoring Team, the H.E.S.S. Collaboration and the MAGIC Collaboration, Science 325 (2009) 444, arXiv: 0908.0511.
- [28] A. Quillen, ApJ 645 (2006) 1092.
- [29] H. Steinle et al., A&A 33 (1998) 97.
- [30] P. Sreekumar et al., Astrop. Phys. 11 (1999) 221.
- [31] Aharonian F. et al., ApJ 614 (2004) 897.
- [32] Aharonian F. et al., A&A 457 (2006) 899.
- [33] V.A. Acciari et al., ApJ 679 (2008) 397, arXiv: 0802.1951.
- [34] A. Franceschini et al., A&A 487 (2008) 837, arXiv: 0805.1841.
- [35] M. M. Reynoso, M. C. Medina, G. E. Romero, A&A 531 A30 (2011).
- [36] Y. Inoue, ApJ 733 (2011) 66 , arXiv: 1103.3946.
- [37] C.J. Willott et al., MNRAS 322 (2001) 536.

- [38] R. Morganti, PASA 27 (2010) 463, arXiv:1003.5568.
- [39] F.P. Israel, Astron. Astrophys. Rev. 8 (1998) 237.
- [40] K.I. Kellermann et al., ApJ 475 (1997) L93.
- [41] Z. Abraham et al., Mon. Not. R. Astron. Soc. 375 (2007) 171.
- [42] A. Markowitz et al., ApJ 665 (2007) 209.
- [43] T.J. Turner et al., ApJ 475 (1997) 118.
- [44] P.R. Wozniak, et al., MNRAS 299 (1998) 449.
- [45] S. Miyazaki et al., Pbl. Astron. Soc. Japan 48 (1996) 801.
- [46] N. Neumayer et al., ApJ 671 (2007) 1329.
- [47] A.D. Tubbs, ApJ 241 (1980) 969.
- [48] A.C. Quillen, PASA 27 (2010) 396, arXiv:0912.0632.
- [49] F.P. Israel et al., A&A 227 (1990) 342.
- [50] D. Espada et al., ApJ 695 (2009) 116.
- [51] A. Marconi et al., ApJ 528 (2000) 276.
- [52] R.A. Nicholson et al., ApJ 387 (1992) 503.
- [53] A.C. Quillen et al., ApJ 391 (1992) 121.
- [54] R. P. Kraft et al., ApJ 698 (2009) 2036.
- [55] R. P. Kraft et al., ApJ 592 (2003) 129.
- [56] R. P. Kraft et al., ApJ 569 (2002) 54.
- [57] M. Kachelriess, et al., New Journal of Physics 11 (2009) 065017.
- [58] M.H. Cohen et al., ApJ 158 (1969) L83.
- [59] H.C. Ford et al., ApJ 435 (1994) L27.
- [60] H.D. Curtis, Pub. Lick. Obs. 13 (1918) 31.
- [61] J. Biretta in: D. Burgarella et al. (Eds.), Astrophysical Jets, Cambridge University Press, (1994) 263. J.A. Biretta & W. Junor, Proc. Natl. Acad. Sci. 92 (1995) 11364.
- [62] R. Malina et al., ApJ 209 (1976) 678.
- [63] E.J. Schreier et al., ApJ 261 (1982) 42.
- [64] C.L. Sarazin, X-ray Emission from Clusters of Galaxies, Cambridge Astrophysics Series, Cambridge University Press, 1988.
- [65] W. Junor et al., Nature 401 (1999) 891.

- [66] C. Ly et al., ApJ 660 (2007) 200.
- [67] F. Aharonian et al, Science 314 (2006) 1424.
- [68] J. Albert et al., ApJ 685 (2008) L23.
- [69] V.A. Acciari et al., ApJ 716 (2010) 819.
- [70] A. Neronov & F.A. Aharonian, ApJ 671 (2007) 85.
- [71] B.M. Sabra et al, ApJ 584 (2003) 164.
- [72] H. Ford & Z. Tsvetanov, Lecture Notes in Physics 530 (1999) 278.
- [73] Z.I. Tsvetanov et al., Proceedings of the M87 Workshop, Ringberg castle, Germany (1998) 15 arXiv: 9803178.
- [74] M.A. Dopita et al., ApJ 490 (1997) 202.
- [75] J.C. Tan et al., ApJ 689 (2008) 775.
- [76] P. E. J Nulsen & H. Böhringer, MNRAS, 274 (1995) 1093.
- [77] H. Böhringer et al, A&A 365 (2001) L181.
- [78] D. Fabricant & P. Gorenstein, ApJ 267 (1983) 535.
- [79] C.S. Reynolds et al., Mon. Not. R. Astron. Soc. 283 (1996) 873.
- [80] S. Hümmer et al., ApJ 721 (2010) 630.
- [81] K. Nakamura and S.T Petcov, Neutrino Mass, mixing and oscillations, in: reference [11].
- [82] M. Ackermann, Astrophys. Space. Sci. 309 (2007) 421.
- [83] R. Abbasi et al., ApJ 732 (2011) 18.
- [84] S. Adrián-Martínez et al, ApJL 743 (2011) L14, arXiv:1108.0292v1.
- [85] B. Hylke et al., Phys. Rev., D78 (2008) 083009.
- [86] F. Halzen and A. O'Murchadha, arXiv: 0802.0887v2.
- [87] F. Halzen, arXiv: 1111.1131v1.
- [88] J. Abraham et al (PAO Collaboration), Science 318 (2007) 939, arXiv: 0711.2256.
- [89] F. Aharonian et al., A&A. 441 (2005) 465.
- [90] R. Abbasi et al., Phys. Rev. D84 (2011) 082001, arxiv: 1104.5187.
- [91] R. Abbasi et al., Proc. of the 32nd ICRC, Beijing (2011) arxiv: 1111.2736.
- [92] J.A. Aguilar et al., Phys.Lett. B696 (2011) 16, arxiv: 1011.3772.
- [93] R. Gandhi et al., Phys. Rev. D58 (1998) 093009-1.
- [94] L.V. Volkova, Sov. J. Nucl. Phys. 31 (1980) 784.



- [95] Luis A. Anchordoqui et al., *Astrop. Phys.* 29 (2008) 1, arxiv: 0703001. J. Abraham et al. (PAO Collaboration), *Astrop. Phys.* 29 (2008) 188, arXiv: 0712.2843.
- [96] J. Carr et al., Proc. of the 30th ICRC, Yucatan, Mexico (2007) ID 0865.